# INTEGRATING PSO AND UKF FOR ATTITUDE ESTIMATION OF RESIDENT SPACE OBJECTS VIA LIGHT CURVES

**Pasquale Bencivenga[(1)], Giovanni Capasso[(1)], Giorgio Isoletta[(1)], Roberto Opromolla[(1)], Giancarmine Fasano[(1)]**

*(1) University of Naples "Federico II", Department of Industrial Engineering, Piazzale Tecchio 80, 80125, Naples, Italy Email: pasquale.bencivenga@unina.it, giovanni.capasso9@studenti.unina.it, giorgio.isoletta@unina.it, roberto.opromolla@unina.it, g.fasano@unina.it*

## ABSTRACT

In the field of Space Situational Awareness, the characterization of Resident Space Objects is a crucial task. Generated by optical systems, Light Curves can provide valuable insights in this context as they depend on the object's shape, material properties, orientation, and position relative to both the Sun and the observer. Thus, it is possible to perform the inverse process to estimate such characteristics exploiting photometric measurements. In this framework, this paper proposes an algorithm to retrieve the attitude of space objects, based on the knowledge of their shapes and reflective properties, by integrating the Particle Swarm Optimization and the Unscented Kalman Filter to exploit their complementary advantages while coping with their individual drawbacks. The effectiveness of the work is evaluated in a simulation environment that can replicate truthful orbital and rotational dynamics evolution and synthetic light curves that account for complex object geometries. Error metrics are computed to compare the estimated attitude histories provided by the algorithm to the true attitude evolution showing good accuracy with significant room for improvement.

## 1 INTRODUCTION

The growing interest in space activities in the last decades has led to a crowded space environment. Indeed, the number of Resident Space Objects (RSOs), constituted of natural and active/inactive artificial objects, has risen consistently escalating the risk of collisions entailing the proliferation of space fragments and possibly leading to the Kessler Syndrome [1, 2]. For these reasons, the Space Situational Awareness (SSA) field, which focuses on the acquisition and analysis of a comprehensive picture about space risks, has gained much importance during the years. Within SSA, the Space Surveillance & Tracking (SST) activities have the objective of monitoring RSOs providing information concerning the position, shape, attitude motion and, in general, properties of space objects. The attitude retrieval of RSOs is one of the most important and challenging activities in SSA. Indeed, it plays a crucial role in understanding the behaviour of RSOs, particularly in the case of non-operational objects. One significant example where attitude estimation is particularly important concerns the re-entry of objects into Earth's atmosphere. Precise knowledge of an object's orientation and motion characteristics can be determining factors in predicting its trajectory. This, in turn, affects the ability to estimate the impact location and potential risks associated with uncontrolled re-entries, which is vital for ensuring the safety of both space assets and populations on the ground. Moreover, attitude estimation can be used to distinct between space debris and active satellites. By analysing the rotational state and stability of an object, it is possible to determine whether it is actively controlled or simply freely rotating due to external torques (i.e., atmospheric drag, solar radiation pressure, gravitational perturbations etc.). This distinction is crucial to avoid misidentifications and improve overall cataloguing accuracy. In addition, understanding the attitude of a space object provides valuable insights into its operational capabilities and intended function. In fact, it is possible to link the attitude of the object to its designed mission, or to make assumptions about possible malfunctioning and threats due to unexpected behaviours.

The characterization of RSOs is accomplished with the help of several types of sensors, either active (e.g., radars) or passive (e.g., telescopes). Passive optical sensors are particularly effective in the characterization of RSOs as they are capable of providing data for faint objects in higher orbits under favourable weather and illumination geometry conditions, without needing the large amounts of power required by active sensors. Specifically, they retrieve the visual apparent magnitude of the target and its collection over time constitutes a Light Curve (LC).

LCs are affected by the reflective properties exhibited by the objects under observation together with its shape and relative geometry between the Sun, the sensor and the object itself. Given these dependencies, it is possible to exploit LCs in an inversion process to retrieve such properties. Focusing on attitude estimation, the LC inversion process presents numerous challenges, mainly related to the non-linearity of the rotational dynamics and to the presence of ambiguities Indeed, a single value of magnitude can be associated with a multitude of conditions in terms of observation geometries and attitude states. Furthermore, a priori knowledge about the object (i.e., its

*Proc. 9th European Conference on Space Debris, Bonn, Germany, 1–4 April 2025, published by the ESA Space Debris Office*
*Editors: S. Lemmens, T. Flohrer & F. Schmitz, (http://conference.sdo.esoc.esa.int, April 2025)*

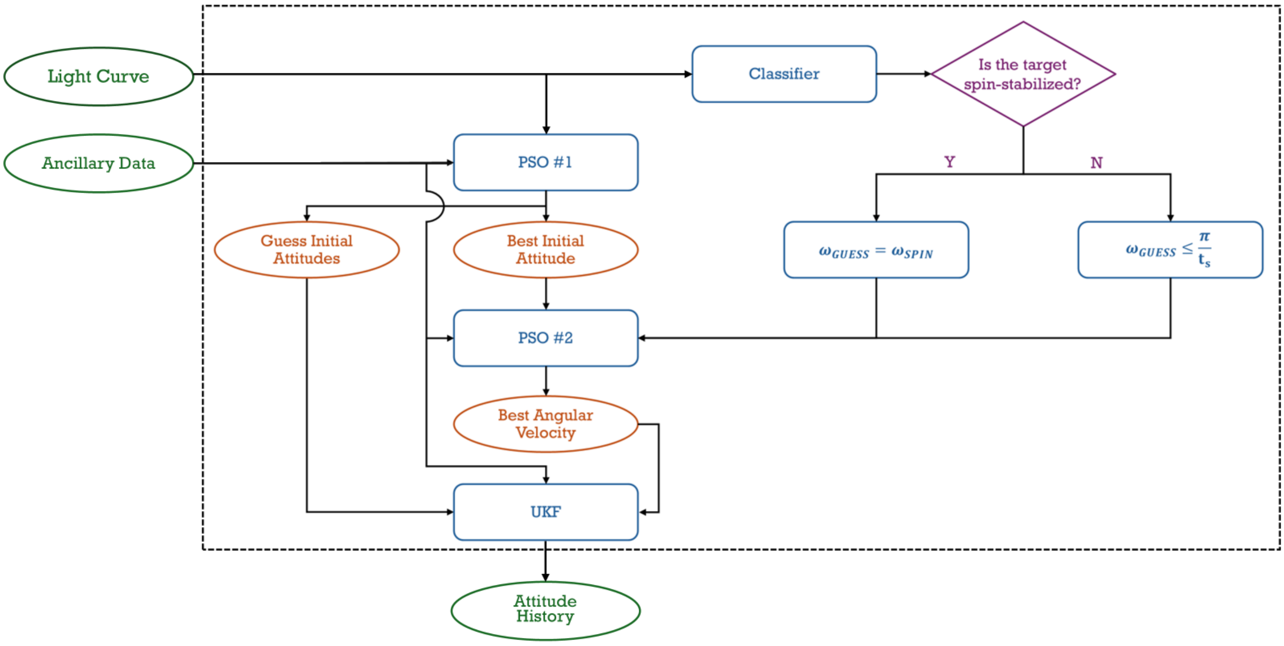


*Figure 1. Workflow of the algorithm*

shape and reflective properties) is required in order to extract information about the target. Different approaches have been proposed so far, involving population-based optimization techniques (e.g., genetic algorithms [3]) and filter-based algorithms (e.g., particle filters [4]).

Reference [5] studied the application of the Particle Swarm Optimization (PSO) technique [6] in this context, implementing a two-phase algorithm to achieve accurate results: a first PSO to find probable attitudes at the initial time instant of the light curve under analysis, and a second one to complete the attitude retrieval starting from a subset of the solutions found by the first PSO.

Reference [7], instead, exploited the Unscented Kalman Filter (UKF) to estimate the attitude history of space objects starting from initial conditions close to the true values.

However, both the techniques have some weakness points. In fact, the PSO requires a large number of particles (and, consequently, a large computational effort) to converge to acceptable results, while the UKF needs an accurate initialization to reach the same purpose. Therefore, this paper proposes a novel architecture based on the combination of the UKF and PSO techniques to exploit their complementary advantages while coping with their individual drawbacks. The proposed architecture uses the PSO to get initial guesses for the state of space objects, which are then used to initialize the UKF in order to reduce the total computational cost.

The remainder of the paper is organized as follows. Section 2 explains how the PSO and UKF are implemented in the algorithmic structure while Section 3 presents the LC simulator and classifier used to produce visual apparent magnitude values and to estimate the attitude motion of the target under observation. Section 4 describes the results obtained. Finally, conclusions are drawn in Section 5.

## 2 METHODOLOGY

Fig. 1 depicts the workflow of the algorithmic architecture. The work makes use of two PSO-based methods so that firstly the LC is processed by a PSO to find a selection of initial attitudes corresponding to the first LC measurement (i.e., the first value of the visual apparent magnitude of the LC) and, afterwards, a second PSO is used to find the best initial angular velocity having in input the best initial attitude from the first PSO and an analysis on the angular velocity's initial guess based on the processing of the LC. Indeed, the LC in input is managed by a classifier, described in Section 3, to estimate the attitude motion of the target. If the target is found to be spin-stabilized, an initial guess for the angular velocity ($\omega_{GUESS}$) is estimated as the rate to complete a spin period ($\omega_{SPIN}$). Otherwise, a maximum value for $\omega_{GUESS}$, related to the Nyquist frequency of the LC and equal to $\frac{\pi}{t_s}$ [5] in which $t_s$ is the sampling rate of the LC, is set. Nonetheless, this branch of the algorithm is described in detail in Subsection 2.1.

The results from the application of the two PSO-based algorithms, constituted of the solutions from the first PSO coupled with the best solution from the second PSO, compose a set of initial guess attitudes and angular velocities that are passed to different UKFs to be refined. This operation is described in Subsection 2.2.

It is fundamental to point out that a LC simulator is used in the implementation of the two PSO-based algorithms and in the application of the UKF. In fact, ancillary data involving characteristics of the propagation and features of the target (in terms of its geometry, reflective properties, etc…) are used as inputs in the LC simulator as it is described in Section 3.

### 2.1 PSO Implementation

The employment of the PSO in this work builds upon other successfully tested applications [5]. As anticipated, a first application of the PSO is used to find the best initial attitudes related to the first measurement of the visual apparent magnitude of the light curve. The objective of the PSO is to minimize a cost function $\mathcal{J}$ which, in this work, assumes the shape of Eq. 1 as it is the relative error between the simulated visual apparent magnitude, $\mathcal{M}_{SIM}$, and the true value at the initial measurement of the LC under analysis, $\mathcal{M}_{TRUE_{IN}}$.

$$\mathcal{J} = \left| \frac{\mathcal{M}_{SIM} - \mathcal{M}_{TRUE_{IN}}}{\mathcal{M}_{TRUE_{IN}}} \right| \tag{1}$$

Each particle $i$ in the swarm is associated with a position $x_i^t$ and a velocity $v_i^t$ at the iteration $t$. Being inspired by the behaviour of flock of birds, the update of the particles' state tries to mimic the inertia, cognitive and social aspects of the swarm motion. Indeed, the velocity is updated following Eq. 2,

$$v_i^{t+1} = wv_i^t + k_1 r_1 (p_i - x_i^t) + k_2 r_2 (s - x_i^t) \tag{2}$$

where $w$ is the inertia weight, $k_1$ and $k_2$ are the cognitive and social coefficient, respectively, $r_1$ and $r_2$ are two random numbers varying between 0 and 1, $p_i$ is the personal best position of the particle, while $s$ is the swarm best position. In particular, $p_i$ and $s$ are the positions having the lowest cost with respect to the $i^{th}$ particle and the swarm, respectively.

The inertia weight usually is set to decrease during the iterations to favor the exploration phase at the beginning of the process and the exploitation phase in the last iterations. The calculation of $v_i^{t+1}$ allows to derive the update of the position, represented by Eq. 3.

$$x_i^{t+1} = x_i^t + v_i^{t+1} \tag{3}$$

The position of a particle is the portrayal of an initial attitude. According to the Euler's theorem, any rotation of a rigid body can be expressed by a rigid rotation $\Phi$ (called Euler's angle) around an axis $e$ (called Euler's axis) which remains unchanged during the given rotation. Thus, Euler's theorem can be used to express the rotation of a space object's BRF with respect to the ECI reference frame. Based on this, attitudes of space objects can be expressed with unit quaternions. A quaternion $\bar{q}$, represented in Eq. 4, is an array composed of four elements in which three elements provide the direction of the Euler's axis, and a fourth element gives information about the rotation angle.

$$\bar{q} = [q_1\ q_2\ q_3\ q_4]^T \tag{4}$$

In this work, the scalar-last notation is used to represent quaternions meaning that the fourth element mentioned before is the last component of the quaternion. The superscript $T$ in Eq. 4 denotes the transposition operation. Eq. 5 explicates the relationship between the quaternion's components and the Euler's axis and rotation angle.

$$\begin{aligned} q_1 &= e_1 \sin\left(\frac{\Phi}{2}\right) \\ q_2 &= e_2 \sin\left(\frac{\Phi}{2}\right) \\ q_3 &= e_3 \sin\left(\frac{\Phi}{2}\right) \\ q_4 &= \cos\left(\frac{\Phi}{2}\right) \end{aligned} \tag{5}$$

Since the PSO is a population-based technique, $np_1$ particles must be initialized with an initial position (i.e., quaternion). Instead of generating random quadruplets, quaternions are created by uniformly sampling values for $e$ and $\Phi$. Considering a sphere of unit radius centred in the BRF, points on the border of the sphere can be found via spherical coordinates thanks to Eq. 6-8.

$$x = sin\theta cos\lambda \tag{6}$$

$$y = sin\theta sin\lambda \tag{7}$$

$$z = cos\theta \tag{8}$$

The triplet $[x, y, z]$ constitutes the position of a point in the BRF, as $\theta$, varying between 0 and $\pi$, and $\lambda$, varying between 0 and $2\pi$, are the azimuth and zenith angle, respectively. Therefore, for the generation of $e$, the domain of $\theta$ is sampled with a value of $\sqrt[4]{np_1}$, while the domain of $\lambda$ is sampled with a value of $4\sqrt[4]{np_1}$ allowing the generation of $4\sqrt{np_1}$ combinations of $e$. Meanwhile, the domain of the rotation angle $\Phi$, equal to $[0,\pi[\ \cup\ ]\pi, 2\pi[$, is sampled with a value of $\frac{\sqrt{np_1}}{4}$ completing the generation of $np_1$ initial quaternions. Although, the rotation angle can assume the value of $\pi$, it is excluded from the domain to sample because it gives ambiguous direction, since with

$\Phi = \pi$ two opposed directions of $e$ would give the same attitude. It may be useful to highlight that, if decimal numbers occur, they are rounded off by excess.

Although representing attitudes in a convenient way, the management of quaternions is affected by some challenges among which the impossibility to add two or more quaternions to obtain a desired attitude since it would violate the norm constraint of the resulting quaternion. For this reason, it is impossible to use directly quaternions in the PSO since it relies on iterative updates of the position of the particles. Indeed, quaternions are converted into the corresponding Euler angles with a 321 sequence.

The conversion operation can create singularities due to the *gimbal lock* problem affecting Euler angles. In particular, singularities occur when the Pitch angle is $\pm 90°$. As a consequence, when the Pitch angle is in the interval $]-91°, -89°[\cup]89°, 91°[$ it is corrected to the nearest extremity of such interval.

After this process, each particle is associated with a quaternion and the relative Euler angles can be used to update the position and velocities of the particles in an additive way, avoiding the mentioned problems.

Finally, after the update, the attitudes are expressed newly into quaternions to be managed by the LC simulator and generate the visual apparent magnitude and the consequent cost for each particle. At the end, solutions are filtered with respect to a threshold.

The best solution is passed to the second PSO which has the objective of looking for a reliable value of the target's angular velocity. The assumption of a torque-free motion is made for the whole duration of the LC. In this case, the PSO is initialized with $np_2$ particles whose positions represent different angular velocities.

Similarly to what happens with the first PSO, instead of generating random vectors, angular velocities are created by uniformly sampling a sphere of radius $\omega_{GUESS}$. If the target is found to be spin-stabilized, $\omega_{GUESS}$ is taken as a reference value for the estimation of all the angular velocities implying that the particles' positions are initialized only with the border of the sphere. Instead, if the target is not found to be spin-stabilized, particles' positions are initialized also with points within the sphere. Thus, the components $[\omega_x, \omega_y, \omega_z]$ of each angular velocity can be calculated with Eq. 9-11.

$$\omega_x = \rho sin\theta cos\lambda \tag{9}$$

$$\omega_y = \rho sin\theta sin\lambda \tag{10}$$

$$z = \rho cos\theta \tag{11}$$

Where $\rho$ is the radius from the origin to the point and varies between 0 and $\omega_{GUESS}$, while $\theta$, varying between 0 and $\pi$, and $\lambda$, varying between 0 and $2\pi$, are the azimuth and zenith angle, respectively. Hence, the domains of $\rho, \theta$ and $\lambda$ are sampled with $\sqrt[3]{np_2}, \frac{\sqrt[3]{np_2}}{2}$ and $2\sqrt[3]{np_2}$ values, respectively. If the target is classified as spin-stabilized, $\rho$ is imposed to be equal to $\omega_{GUESS}$ and the domains of $\theta$ and $\lambda$ are sampled with $\frac{\sqrt{np_2}}{2}$ and $2\sqrt{np_2}$ values. As it happens in the first PSO, if decimal numbers occur, they are rounded off by excess. After the initialization phase, the best solution of the first PSO is propagated with the assumption of a torque-free motion until the end of the LC with the angular velocities of the particles. Thus, each particle's cost $\mathcal{J}$ is found as the relative error between the simulated and true visual apparent magnitude corresponding to the last sample of the LC, as it is depicted in Eq. 12.

$$\mathcal{J} = \left|\frac{\mathcal{M}_{SIM} - \mathcal{M}_{TRUE_{LAST}}}{\mathcal{M}_{TRUE_{LAST}}}\right| \tag{12}$$

Afterwards the process continues with the update of the velocities and positions until the end of the iterations. Additionally, when the target is classified as spin-stabilized, corrections on the update of the particles' positions are made to adjust the norm to the value of $\omega_{GUESS}$.

## 2.2 UKF Implementation

Different UKFs is set up to take into account the solutions from the first PSO and the best angular velocity from the second PSO. The quaternions are converted into the respective Euler angles which, together with the angular velocity, constitute the 6-dimensional state $x$. However, to capture the process and measurement noise more accurately, the state is augmented to 13 dimensions, as shown in Eq. 13 (where $x^E$ denotes the Euler angles), since the process noise matrix $Q$ is defined a 6x6 matrix while the measurement noise matrix $R$ reduces to a scalar as the only measurement is the visual apparent magnitude. $R$ is particularly important in the filter because it accounts for the missing noise addition in the generation of visual apparent magnitude values, as it is described in Section 3.

$$x^a = [x^E \; \omega \; 0_{6x1} \; 0] \tag{13}$$

Therefore, $(2L+1)$ the augmented sigma points $\chi$ are generated for a total of 27 points as $L$ is the dimension of the augmented state. The calculation of the sigma points is shown in Eq. 14-16.

$$\chi_0^a = x^a \tag{14}$$

$$\chi_i^a = x^a + \sqrt{(L+\lambda)P^a} \qquad i = 1, \dots, L \tag{15}$$

$$\chi_i^a = x^a - \sqrt{(L+\lambda)P^a} \qquad i = L+1, \dots, 2L \tag{16}$$

Where $P^a$ is the augmented state covariance matrix given by Eq. 17, $\lambda$ is a scaling parameter given by Eq. 18 in which $\alpha$ and $\kappa$ are the tuning parameters of the UKF together with $\beta$, regulating the spread of the sigma points distribution.

$$P^a = \begin{pmatrix} P_x & 0 & 0 \\ 0 & Q & 0 \\ 0 & 0 & R \end{pmatrix} \tag{17}$$

$$\lambda = \alpha^2(L+\kappa) - L \tag{18}$$

In Eq. 17, $P_x$ is the 6x6 state covariance. It may be useful to evidence that the square roots appearing in Eq. 15-16 are calculated using the Cholesky decomposition.

After the initialization, the Euler angles components of the sigma points are converted into the corresponding quaternions, propagated until the next filter step under the assumption of a torque-free motion, and re-converted into Euler angles. This operation occurs at each step so that the first 6 components of the propagated augmented sigma points, denoted as $\chi^x_{i_{k|k-1}}$, are used in Eq. 19-20 to predict the a priori state and state covariance matrix.

$$\hat{x}_k^- = \sum_{i=0}^{2L} w_i^m \chi^x_{i_{k|k-1}} \tag{19}$$

$$P_{x_k}^- = \sum_{i=0}^{2L} w_i^c \left(\chi^x_{i_{k|k-1}} - \hat{x}_k^-\right)\left(\chi^x_{i_{k|k-1}} - \hat{x}_{k+1}^-\right)^T + Q \tag{20}$$

Where $w_i^m$ and $w_i^c$ are the weights accounting for the mean and the covariance and are expressed in Eq. 21-23, respectively

$$w_0^m = \frac{\lambda}{L+\lambda} \tag{21}$$

$$w_0^c = \frac{\lambda}{L+\lambda} + (1-\alpha^2+\beta) \qquad i = 1, \dots, 2L \tag{22}$$

$$w_0^m = w_0^c = \frac{1}{2(L+\lambda)} \qquad i = 1, \dots, 2L \tag{23}$$

The propagated sigma points are exploited to obtain the prediction of the visual apparent magnitude relative to the successive filter step as it is expressed in in equation Eq. 24.

$$Y_{i_{k|k-1}} = h\left(\chi^x_{i_{k|k-1}}\right) + \chi^{v_R}_{i_{k|k-1}} \tag{24}$$

Where $Y_{i_{k|k-1}}$ represents the expected measurements for all the sigma points, $h$ is measurement function which englobes the LC simulator while $\chi^{v_R}_{i_{k|k-1}}$ is the measurement component of the augmented sigma points. The individual expected measurements for the different sigma points are then combined using the weighting scheme to determine the mean expected measurement $\tilde{y}_k$ as it is done in Eq. 25.

$$\tilde{y}_k = \sum_{i=0}^{2L} w_i^m Y_{i_{k|k-1}} \tag{25}$$

Hence, the measurement covariance matrix $P_{y_k}$ and the state-measurement cross-covariance matrix $P_{x_k y_k}$ are calculated as follows in Eq. 26-27 and used to calculate the Kalman gain matrix $K_k$ as it is done in Eq. 28.

$$P_{y_k} = \sum_{i=0}^{2L} w_i^c \left(Y_{i_{k|k-1}} - \tilde{y}_k\right)\left(Y_{i_{k|k-1}} - \tilde{y}_k\right)^T + R \tag{26}$$

$$P_{x_k y_k} = \sum_{i=0}^{2L} w_i^c \left(\chi^x_{i_{k|k-1}} - \hat{x}_k^-\right)\left(Y_{i_{k|k-1}} - \tilde{y}_k\right)^T \tag{27}$$

$$K_k = P_{x_k y_k} P_{y_k}^{-1} \tag{28}$$

The superscript $(-1)$ in Eq. 28 denotes the inversion operation. The UKF can be set to work with a sampling rate much lower than the sampling time of the LC. Thus, it is possible to have the absence of a true measurement at certain filter steps. If this case occurs, the a posteriori estimated state $\hat{x}_k^+$ is imposed to be equal to the a priori state $\hat{x}_k^-$ as it is impossible to correct the predicted measurement. Meanwhile, if there is a true measurement $\mathcal{M}_{TRUE}$ available, the a posteriori estimated state $\hat{x}_k^+$ and state covariance matrix $P_{x_k}^+$ are calculated with Eq. 29-30.

$$\hat{x}_k^+ = \hat{x}_k^- + K_k\left(\tilde{y}_k - \mathcal{M}_{TRUE_k}\right) \tag{29}$$

$$P_{x_k}^+ = P_{x_k}^- + K_k P_{y_k} K_k^T \tag{30}$$

The UKF continues with the described operations until the end of the LC.

## 3 LC SIMULATOR AND CLASSIFIER

As has been stated, the implementation of the PSO and UKF necessitates a simulator to obtain realistic magnitude values. Thus, a light curve generator has been developed which is part of a larger software tool involving an orbital and attitude propagator built upon [8].

The LC simulator, based on [9], accepts the following inputs:

- Geometric model and reflectivity characteristics of the target: the target can be represented either by importing a CAD model of any complexity or by combining basic shapes, with their surfaces discretized into a triangular mesh. Each triangle is characterized by an area, a normal unit vector, and the diffusive and specular reflectivity coefficients.
- Initial state vector: this includes the target's orbital and attitude information. The position is defined in the

Earth-Centered Inertial (ECI) frame, while the angular velocity is given in the Body Reference Frame (BRF); the target's orientation is described by a quaternion relating the BRF to the ECI.

- Start and end epochs for the simulation period of interest.
- Properties of optical sensors, such as their Field of View and Signal-to-Noise Ratio (SNR).
- Geodetic coordinates for ground-based sensors.
- Orbital parameters for space-based sensors.

Hence, in output, the LC simulator provides light curves of the target as observed by each sensor during the observation periods.

The generation of light curves is enabled by employing the Cook-Torrance model [10] to simulate the target's optical behaviour. Here, the visual apparent magnitude of the target being observed is indicated by $\mathcal{M}$ and is modelled in Eq. 31.

$$\mathcal{M} = -26.7 - 2.5 \cdot \log_{10}\left(\frac{\mathcal{B}}{\mathcal{B}_{SUN}}\right) \quad (31)$$

The value of -26.7 depicts the visual apparent magnitude of the Sun, while $\mathcal{B}$ and $\mathcal{B}_{SUN}$, representing irradiances $[\frac{W}{m^2}]$, denote the brightness values of the target and the Sun, respectively. These values are calculated using the Cook-Torrance model which accounts for the contributions from all illuminated and visible meshed sections of the target. A facet is considered visible if it satisfies two simultaneous conditions: it is lit by the Sun and it is within the sensor's line of sight. Finally, the classification of the LC to estimate the attitude motion of the target is made by means of a spectrum analysis performed via the Lomb-Scargle Periodogram (LSP) [11] and the Phase Dispersion Minimization (PDM) [12].

In this work, the LC simulator is used also to generate a synthetic LC to be employed as the input of the algorithmic architecture. Nonetheless, the production of visual apparent magnitude values in the generation of the input and in the implementation of the two PSO-based techniques and of the UKF is different. Indeed, noise is added in the origination of the LC to analyse while this does not happen in the rest of the algorithm. In particular, in the synthesis of the LC to analyze noise is added to the photometric measurements with a WGN model in which the standard deviation is set equal to the mean of the measurements of brightness obtained by the sensor which collects the photometric measurements, and divided by $\frac{SNR}{10}$ where SNR is the Signal-to-Noise Ratio of the observing sensor.

## 4 RESULTS

This section presents the application of the pipeline to a target modelled as a cylinder-shaped object whose extremities are hemispherical in order to emulate the structure of a rocket body. Tab. 1 shows the geometric characteristics of the target. The initial epoch of the propagation is the 24th of March 2003 at 13:30:26 with the propagation lasting 9 hours. The initial orbital parameters are listed in Tab. 2.

*Table 1: Characteristics of the target's model*

| **Feature** | **Cylinder body** | **Hemispherical end caps** |
|---|---|---|
| **Number of facets** | 100 | 100 |
| **Height [m]** | 1.5 | 1.5 |
| **Radius [m]** | 9 | 1 |

*Table 2. Target's initial orbital parameters*

| **a [km]** | **e** | **RAAN [°]** | **i [°]** | **AoP [°]** |
|---|---|---|---|---|
| 7302.1 | 0.06 | 73.9 | 30.3 | 327.2 |

The target's initial quaternion is $q_{IN} = [-0.4401, -0.3532, -0.1847, 0.8047]^T$ while its initial angular velocity is $\omega_{IN} = [10, -0.2, -0.3]^T\ °/s$ having a norm of 10.01 °/s. Fig. 3 depicts the simulated light curve with the ground-based telescope whose characteristics are listed in Tab. 3 where the longitude, latitude and altitude values refer to the WGS84 model of the Earth. The dusk angle is defined as the minimum angle below the local horizon of the sensor at which the Sun must be for an object to be observable, while the mask angle is the minimum elevation angle above the observer's horizon that an object must have in order to be observable. The LC in input is classified to estimate the target's attitude motion. In particular, the target's is assessed to be spin-stabilized, and a spin rate of 10.1 °/s is found. This value is used as the reference angular velocity norm in the second PSO so that all the angular velocities computed by the algorithm have a norm of 10.1 °/s.

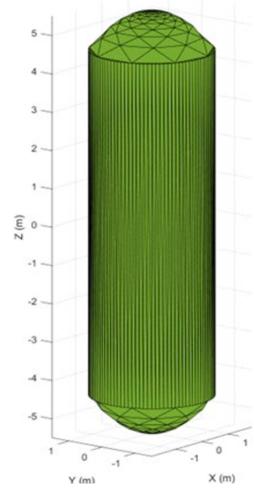


*Figure 2. Rocket body model*

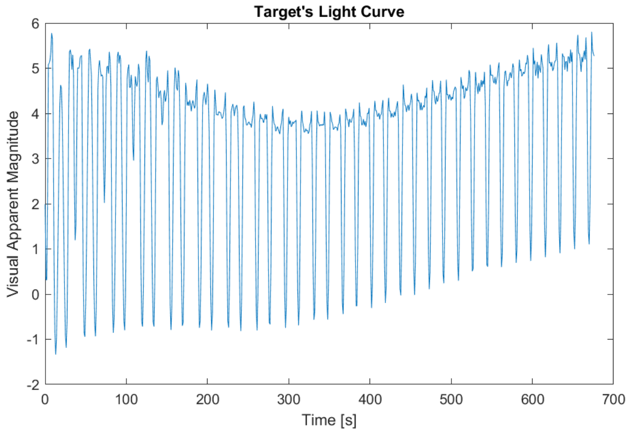


*Figure 3: Target's light curve*

*Table 3. Sensor's characteristics*

| Longitude | Latitude | Altitude | Dusk Angle | Mask Angle | SNR |
|---|---|---|---|---|---|
| -16.93 ° | 32.74° | 1818 m | 4° | 10° | 20 |

Concerning the analysis with the two PSO-based algorithms, in both cases the inertia weight is modified at each iteration by a multiplication with a damping coefficient equal to 0.97 in both the PSO-based techniques. This is done to impose a larger value to the inertia weight with respect to most PSO applications. As a result, this causes an accentuation on a first exploration phase by the particles in order to avoid local minima due to the ambiguity nature of the phenomenon.

The entire simulation has been run using MATLAB R2024b on a personal computer equipped with an 11th Gen Intel Core i9-11900 processor, operating at 2.5 GHz, and 32 GB of RAM.

The first PSO analysis is conducted with $np_1 = 10000$ particles, an inertia weight $w = 1$ and with both $k_1$and $k_2$ equal to 0.8. The number of iterations has been fixed to 50. The particles' velocities are initialized with random 3x1 vectors having a norm of 5 °. The results are finally filtered with a threshold of $10^{-4}$ on the cost, giving a total of 677 solutions with a processing time of 25 minutes.

The best quaternion found is $q = [-0.436, -0.059, -0.604, 0.663]^T$ which is put in input in the second PSO algorithm initialized with $np_2 = 1000$, an inertia weight $w = 1$ and with both $k_1$and $k_2$ equal to 0.8. The best angular velocity found is equal to $\omega = [-9.45, -2.82, -2.19]^T$ $°/s$ in a total processing time of 3 minutes and in a total of 30 iterations.

The solutions found by the first PSO and the best angular velocity found by the second PSO are given in input to the UKF which is set with the values listed in Tab. 4 where $\nu_Q$, $\nu_R$, $\nu_{P_{x_0}}$ multiply a 6x6, 1x1, 6x6 identity matrices to initialize $Q$, $R$, and $P_{x_0}$. The frequency of the filter is set to 1 Hz and its analysis lasts 50 minutes.

*Table 4. UKF settings*

| $\alpha$ | $\beta$ | $\kappa$ | $\nu_Q$ | $\nu_R$ | $\nu_{P_{x_0}}$ |
|---|---|---|---|---|---|
| 0.01 | 2 | 0 | $10^{-3}$ | 0.3 | $10^{-6}$ |

Although exhibiting a very low initial error giving the threshold on the solutions provided by the first PSO, the results of the UKF show large errors either for the visual apparent magnitude estimation, with a mean error of 3.4, or for the attitude history prediction, with a mean error of 67° on the Yaw component, 83° on the Pitch component and 101° on the Roll component. The motivation under such large mean errors is linked to the ambiguous nature of the phenomenon which leads to multiple valid initial attitudes even if they are far from the truth since they exhibit the same visual apparent magnitude. On the other hand, not all the results need to be discarded since the filter has proven its capability to estimate the attitude history of the target with certain initial attitudes. Indeed, Fig. 4 depicts the estimated visual apparent magnitude of the best solution found by the UKF (with an initial quaternion equal to q = $[-0.874, -0.123, -0.389, 0.264]^T$) with respect to the true visual apparent magnitude. It can be seen that the filter's accurately follows the behavior of the signal as it is further demonstrated with Fig. 5 in which the absolute error and the absolute percentage error are represented. In particular, the mean error is equal to 0.09 while the median error is 0.04.

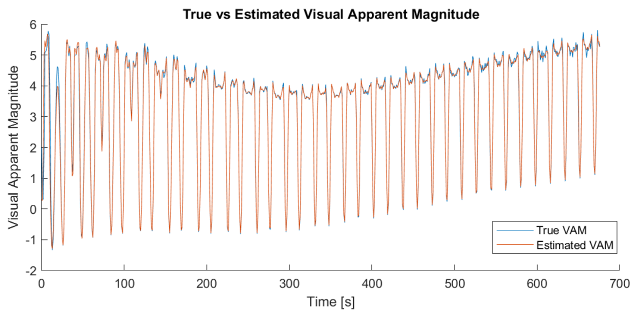


*Figure 4. True and estimated visual apparent magnitude*

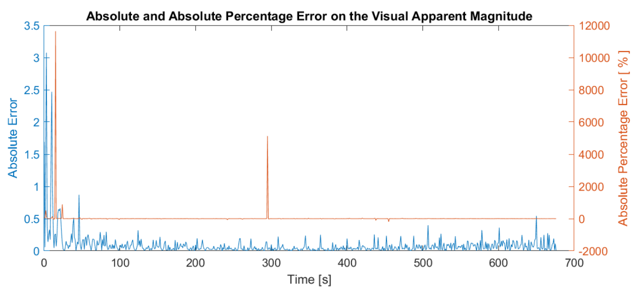


*Figure 5. Absolute and absolute percentage error on the visual apparent magnitude*

In this case, the low errors on the estimation of the visual apparent magnitude also reflect in an accurate estimation on the attitude history. As a matter of fact, Fig. 6-8 show the estimated Yaw, Pitch and Roll components of the Euler angles' history with respect to the true values. The difference between the estimated and true values can be better appreciated in Fig. 9-11 in which the absolute errors are depicted. It can be noticed that the errors on the three angles are stable during the whole signal's window portraying a mean error of 2.1 °, 0.6° and 4.9° on the Yaw, Pitch and Roll angles, respectively.

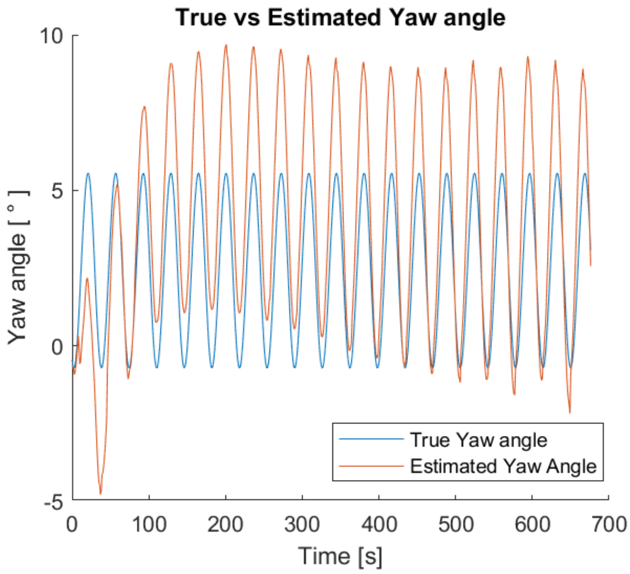


*Figure 6. Estimated and true Yaw angle history*

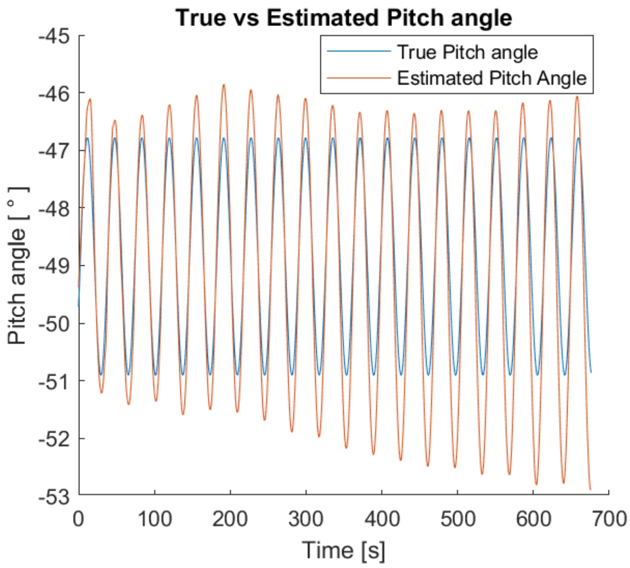


*Figure 7. Estimated and true Pitch angle history*

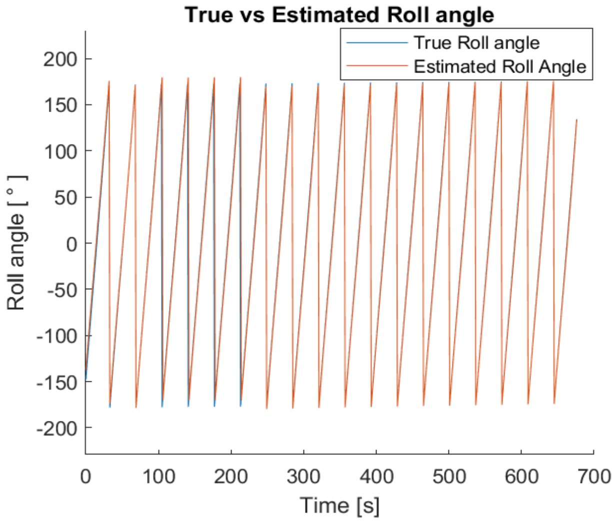


*Figure 8. Estimated and true Roll angle history*

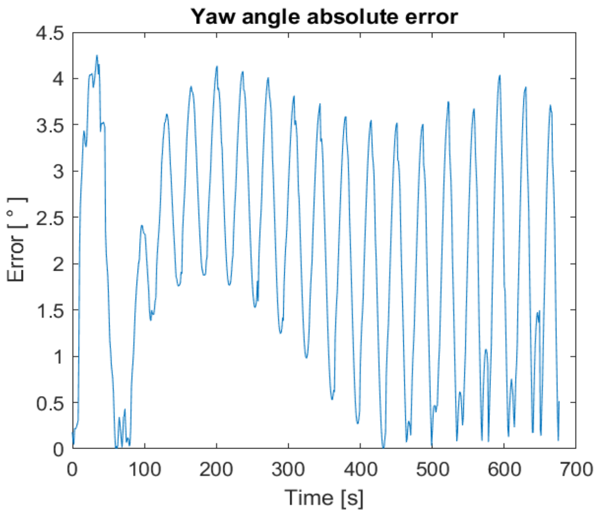


*Figure 9. Absolute error on the Yaw angle*

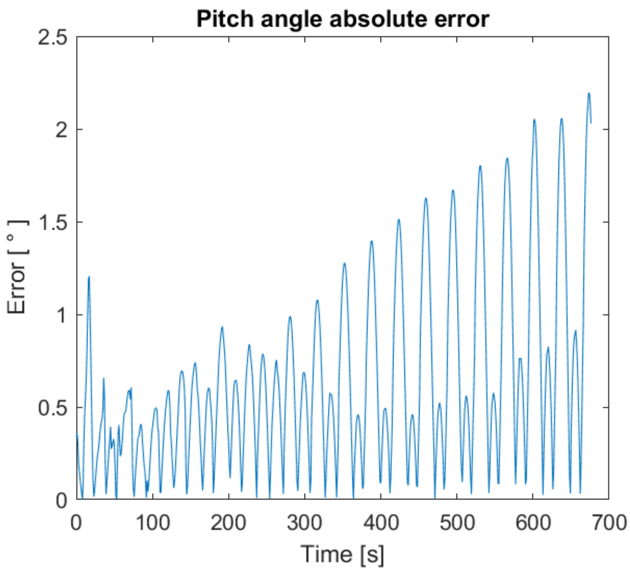


*Figure 10. Absolute error on the Pitch angle*

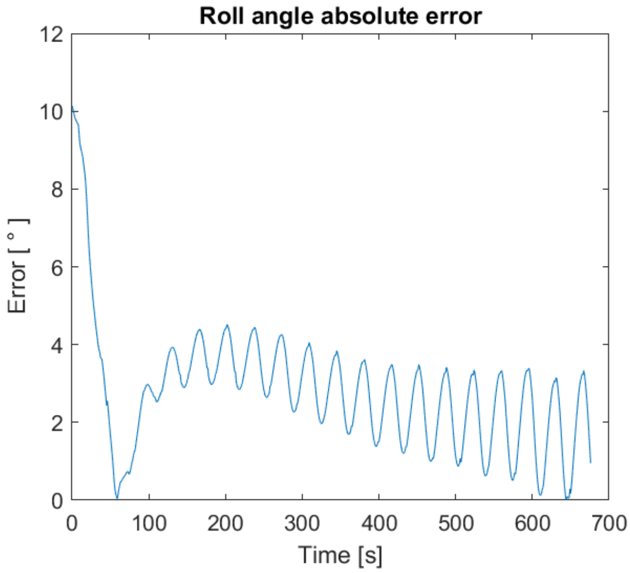


*Figure 11. Absolute error on the Roll angle*

## 5 CONCLUSIONS

By combining the Particle Swarm Optimization and the Unscented Kalman Filter, this work offers a novel method for the estimation of the attitude of Resident Space Objects using light curves. The implementation of the PSO has proved the theoretical advantages of its integration with the UKF providing accurate initial guesses significantly improving the UKF initialization. However, a lot of solutions provided by the first PSO algorithm are discarded due to the ambiguity of the problem to solve. The simple geometry of the test case may have accentuated such effect. Thus, to improve this situation, a more complex geometry model may be implemented. Furthermore, the UKF can be modified into its multiplicative variant to be able to manage directly quaternions instead of Euler angles. In addition, the tuning of the UKF can be refined via the use of another PSO-based approach to find the best values to set the filter. Finally, the LC simulator may be validated in order to test the pipeline in real scenarios.


## 6 AKNOWLEDGEMENTS

This work has been developed within the project "Attività tecnico-scientifiche di supporto a C-SSA/ISOC e simulazione di architetture di sensori per SST" funded by the Italian Space Agency (ASI).


## 7 REFERENCES


1. L. Miraux. (2022). Environmental limits to the space sector's growth. *Science of The Total Environment* 806 150862.

2. D.J. Kessler, & B.G. Cour-Palais. (1978). Collision frequency of artificial satellites: The creation of a debris belt. *Journal of Geophysical Research: Space Physics* 83(A6) 2637–2646.

3. F. Piergentili, F. Santoni, & P. Seitzer. (2017). Attitude Determination of Orbiting Objects from Lightcurve Measurements. *IEEE Transactions on Aerospace and Electronic Systems* 53(1) 81–90.

4. R. Linares, J. Crassidis, & M. Jah. (2016). *Particle filtering light curve based attitude estimation for non-resolved space objects*.

5. A. Burton, L. Robinson, & C. Frueh. (2024). Light curve attitude estimation using particle swarm optimizers. *Advances in Space Research* 74(11) 5619–5638.

6. J. Kennedy, & R. Eberhart. Particle swarm optimization. *Proceedings of ICNN'95 - International Conference on Neural Networks* 4 1942–1948.

7. A.J. Bernard. (2021). Attitude and Reflection Parameter Estimation of Resident Space Objects Using Ground-Based Photometry. *All Graduate Theses and Dissertations, Spring 1920 to Summer 2023*.

8. G. Isoletta, R. Opromolla, & G. Fasano. (2025). Attitude motion classification of resident space objects using light curve spectral analysis. *Advances in Space Research* 75(1) 1077–1095.

9. P. Bencivenga, G. Isoletta, R. Opromolla, & G. Fasano. (2024). *Attitude Motion Characterization of Resident Space Objects via Fusion of Ground-based and Space-based Light Curves*.

10. R.L. Cook, & K.E. Torrance. (1982). A Reflectance Graphics Model for Computer. *ACM Transactions on Graphics* 1(1) 7–24.

11. J.T. VanderPlas. (2018). Understanding the Lomb–Scargle Periodogram. *The Astrophysical Journal Supplement Series* 236(1) 16.

12. R.F. Stellingwerf. (1978). Period Determination Using Phase Dispersion Minimization. *The Astrophysical Journal* 224 953–960.